Chinese Chemical Letters 37 (2026) 111721

Contents lists available at ScienceDirect

Chinese Chemical Letters

journal homepage: www.elsevier.com/locate/cclet

Indolizine-benzophenone hybrid acceptors enable TADF materials for bioimaging and photodynamic therapy in living cells

Hui Guo[a,b], Wen-Wen Li[a], Mei-Yin Wu[a], Jian-Bo Hu[a], Jun Wang[a], Yun Liu[a,*], Yang Zou[c], Chu-Luo Yang[c,*], Kai-Lu Zheng[a,*]

[a] Guangdong Provincial Key Laboratory of Natural Drugs Research and Development, School of Pharmacy, Guangdong Medical University, Dongguan 523808, China
[b] Department of Pharmacy, Shantou Central Hospital, Shantou 515031, China
[c] Shenzhen Key Laboratory of New Information Display and Storage Materials, College of Materials Science and Engineering, Shenzhen University, Shenzhen 518060, China

ARTICLE INFO

Article history:
Received 10 April 2025
Revised 12 August 2025
Accepted 14 August 2025
Available online 14 August 2025

Keywords:
Indolizine-benzophenone
Thermally activated delayed fluorescence
Aggregation-induced emission
Photodynamic therapy
Bioimaging

ABSTRACT

Thermally activated delayed fluorescence (TADF) emitters show great potential in photodynamic therapy (PDT) and bioimaging, leveraging their structural adaptability, efficient reverse intersystem crossing (RISC), robust photosensitizing capability, and high photoluminescence quantum yields (PLQYs). Herein, we developed a new class of donor–acceptor–donor (D-A-D)-type TADF materials by connecting the highly twisted indolizine-benzophenone electron acceptors with a series of electron donors including phenoxazine, phenothiazine and 9,9-dimethyl-9,10-dihydroacridine. These materials exhibit enhanced TADF properties, aggregation-induced emission (AIE), alongside high reactive oxygen species (ROS) generation efficiency, effectively mitigating aggregation-caused quenching observed in traditional fluorophores. Among them, IDP-p-PXZ, incorporating the phenoxazine donor, stands out with the smallest singlet–triplet splitting energy (ΔE_{ST}) and the highest spin-orbit coupling matrix elements (SOCMEs). Upon encapsulation into 1,2-distearoyl-*sn*–glycero-3-phosphoethanolamine-*N*-[methoxy(polyethylene glycol)-2000] (DSPE-PEG2000) nanoparticles (NPs), IDP-*p*-PXZ demonstrates extended delayed fluorescence lifetimes in air, an exceptionally fast intersystem crossing (ISC) rate constant (k_{ISC}) of 3.4×10^7 s^{-1}, and a radiative rate constant (k_r) of 5.05×10^6 s^{-1}. These NPs exhibit superior biocompatibility, efficient cellular internalization, and potent ROS production, enabling effective simultaneous PDT and confocal fluorescence imaging in HeLa cells.

© 2025 Published by Elsevier B.V. on behalf of Chinese Chemical Society and Institute of Materia Medica, Chinese Academy of Medical Sciences.

Thermally activated delayed fluorescence (TADF) emitters are a class of pure organic luminescent materials with relatively small singlet–triplet splitting energy (ΔE_{ST}), which allow for efficient reverse intersystem crossing (RISC) process to upconvert excitons from non-radiative T_1 to radiative S_1 state using ambient thermal energy [1–3]. These features render the TADF emitters high photoluminescence quantum yields (PLQYs) and long-lived excited states, which can be promising in applications in organic light-emitting diodes [4,5], bioimaging [6], biosensors, and nanomedicine [7–10]. By virtue of the specific photophysical features, TADF materials have drawn great attention in biomedical applications in recent years. For example, the TADF molecule AI-Cz conjugated with a bacteria 16S rRNA-targeting neomycin was successfully applied in confocal fluorescence imaging and time-resolved fluorescence imaging in cells and tissues [11]. The near-infrared emitted boron difluoride-crocin polymer exhibiting TADF feature was incorporated into water-soluble polymer dots (Pdots) to obtain near-infrared (NIR) emissive nanoparticles (NPs) CzBN-co-DtaB. These Pdots were combined with antibodies, causing SK-BR3 human breast cancer cells to produce immune fluorescent labeling [12], which is the first example of a biomedical imaging probe for human SK-BR3 cells.

Photodynamic therapy (PDT) is a non-invasive and damage-free treatment method that has been successfully applied in the clinical treatment of certain cancers [13–18]. The underlying principle of PDT involves the utilization of photosensitizers (PSs) that exhibit low dark toxicity, ensuring minimal harm to healthy tissues in the absence of light. Upon photoexcitation, the PSs are activated, generating cytotoxic reactive oxygen species (ROS) such as singlet oxygen ($^1O_2$), which selectively damage tumor cells. No-

* Corresponding authors.
E-mail addresses: liuyun0171@whu.edu.cn (Y. Liu), clyang@szu.edu.cn (C.-L. Yang), kailuzheng@gdmu.edu.cn (K.-L. Zheng).

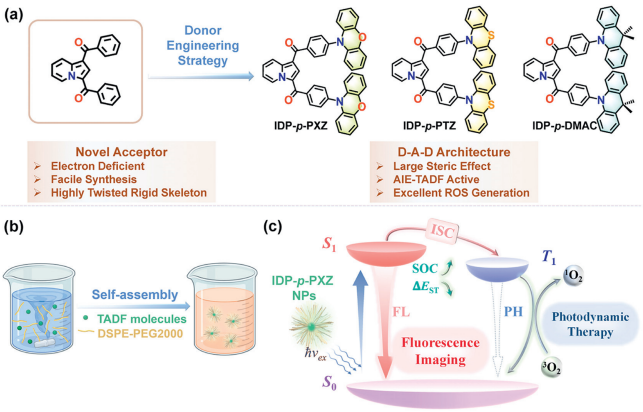
https://doi.org/10.1016/j.cclet.2025.111721
1001-8417/© 2025 Published by Elsevier B.V. on behalf of Chinese Chemical Society and Institute of Materia Medica, Chinese Academy of Medical Sciences.

tably, TADF materials, characterized by a small ΔE_{ST} and a rapid intersystem crossing (ISC) process, are particularly advantageous for this purpose. These materials can easily undergo the ISC process to populate the triplet state T_1, thus transferring energy to ground state $^3O_2$ and producing cytotoxic $^1O_2$ [19,20]. This unique combination of properties makes TADF materials highly promising for advancing PDT applications. In 2021, Huang group reported lysosome-targeting TADF NPs (TPE-AQ NPs) for human tongue squamous cell carcinoma (CAL27) and human tongue squamous cell carcinoma (HSC3), which released ROS under 450 nm laser irradiation, showing good *in vitro* cell and mouse tumor PDT effects [21]. Recently, Song and coworkers found that encapsulating TADF PSs with bovine serum albumin could significantly promote the type I PDT process to generate a large amounts of superoxide anion ($O_2^{\bullet-}$), demonstrating a significant enhancement in the PDT killing effect on tumor cells under hypoxic conditions *in vitro* [22].

The unique properties of aggregation-induced emission (AIE) and TADF offers a promising pathway to develop advanced luminescent materials for applications such as bioimaging and PDT [20,23–29]. Materials exhibiting both AIE and TADF properties can effectively suppress nonradiative transitions and shield TADF molecules from surrounding oxygen, thereby enhancing luminescence efficiency. Rigid scaffold structures with highly twisted conformations are particularly advantageous, as they promote well-separated distributions of the highest occupied molecular orbital (HOMO) and the lowest unoccupied molecular orbital (LUMO), minimizing detrimental $\pi-\pi$ stacking interactions. This design strategy has proven effective for developing AIE-active TADF emitters.

Benzophenone, a classic organic molecule characterized by its rigid planar structure and strong electron-withdrawing properties, has established itself as a highly effective acceptor unit in the design of AIE-TADF materials. On the other hand, indolizine derivatives are renowned for their diverse pharmacological properties, including antioxidant and anticancer activities [30–32], and hold significant potential for the development of versatile fluorogenic bioprobes. Building on these advantages, this work introduces benzoyl-substituted indolizine as a novel electron acceptor in the design of AIE-TADF emitters. The integration of a rigid yet relatively torsional framework into the molecular structure ensures well-separated distributions of the HOMO and the LUMO, effectively minimizing $\pi-\pi$ stacking interactions. This innovative design not only enhances the luminescence efficiency of the materials but also opens new avenues for their application in bioimaging and PDT.

In this work, indolizine-benzophenone was established as a potent platform for AIE-active TADF molecules, and three TADF emitters, namely indolizine-1,3-diylbis((4-(10*H*-phenoxazin-10-yl)phenyl)methanone) (IDP-*p*-PXZ), indolizine-1,3-diylbis((4-(10*H*-phenothiazin-10-yl)phenyl)methanone) (IDP-*p*-PTZ), and indolizine-1,3-diylbis((4-(9,9-dimethylacridin-10(9*H*)-yl)phenyl)methanone) (IDP-*p*-DMAC), were synthesized by donor engineering strategy to form donor–acceptor–donor (D-A-D) architectures (Scheme 1). The developed TADF molecules display a highly twisted molecular configuration with small ΔE_{ST} values, large spin-orbit coupling matrix elements (SOCMEs), distinct AIE, and remarkable capability for ROS generation. Since the phenoxazine (PXZ) is a donor with a more planar structure as well as stronger electron-donating ability than those of phenothiazine (PTZ) or 9,9-dimethyl-9,10-dihydroacridine (DMAC), IDP-*p*-PXZ demonstrated reduced intramolecular motion and thus enhanced photoluminescence (PL) performance. In alignment with these, IDP-*p*-PXZ NPs prepared with 1,2-distearoyl-*sn*–glycero-3-phosphoethanolamine-*N*-[methoxy(polyethylene glycol)-2000] (DSPE-PEG2000) showed good biocompatibility and exciton



Scheme 1. (a) The molecular design concept of indolizine-benzophenone acceptor-based TADF emitters. (b) The preparation of TADF NPs. (c) Mechanism of IDP-*p*-PXZ NPs mediated fluorescence imaging and photodynamic therapeutic.

dynamics data, achieving confocal fluorescence imaging and photodynamic therapeutic applications in HeLa cells.

We designed and synthesized the three TADF molecules by introducing indolizine-1,3-diylbis(phenylmethanone) (IDP) unit as an identical electron acceptor. According to the coupling kinds of donors, they are named as IDP-*p*-PXZ, IDP-*p*-PTZ, and IDP-*p*-DMAC. The synthetic routes of these compounds are shown in Scheme S1 (Supporting information). The key intermediate of indolizine-1,3-diylbis((4-bromophenyl)methanone) (4,4′-2Br-IDP) was prepared by a one-pot transition-metal-free cascade oxidation/1,3-dipolar cycloaddition reaction between pyridinium salts and DMSO [33]. IDP-*p*-PXZ, IDP-*p*-PTZ and IDP-*p*-DMAC were synthesized through a straightforward palladium-catalyzed C–N coupling reaction of 4,4′-2Br-IDP with PXZ, PTZ, and DMAC. Their chemical structures are characterized by the ^1H and ^{13}C nuclear magnetic resonance (NMR), single-crystal X-ray diffraction, and high-solution mass spectroscopy.

Theoretical calculations were first performed based on single crystal structures to predict the molecular characteristics. Fig. S1 (Supporting information) showed their frontier molecular orbitals (FMOs), energy levels and the excited state features by using density functional theory (DFT) calculations. Ground state optimization used B3LYP-GD3(BJ) function with split valence polarization (def2-SVP) basis set while excited state using PBE1PBE function with def2-SVP basis set. All compounds featured a twisted structure with near perpendicular configuration between the donor and the acceptor unit at the optimized geometry, and the corresponding dihedral angles are 81.0° and 81.6° for IDP-*p*-PXZ, 82.5° and 88.2° for IDP-*p*-PTZ, and 81.3° and 83.4° for IDP-*p*-DMAC. The large twisted configurations endowed them a well-separated HOMO and LUMO distributions. As shown in Fig. S1, the HOMOs were localized on the donor groups and the LUMOs were mainly located on the indolizine-benzophenone acceptor groups. As expected, all the three molecules exhibited small ΔE_{ST} values of 0.07 eV for IDP-*p*-PXZ, 0.14 eV for IDP-*p*-PTZ, and 0.29 eV for IDP-*p*-DMAC, suggesting the high potential as TADF emitters. Notably, IDP-*p*-PXZ showed the smallest ΔE_{ST} (0.07 eV) and the largest SOCME between S_1 and T_1 ($<S_1|\hat{H}_{SOC}|T_1>$) (0.31 cm^{-1}) among the three emitters, which is beneficial for the efficient ISC process to enhance triplet sensitization, indicating a good potential in the generation of ROS in PDT.

To gain further insights into the three molecules, X-ray single crystals analysis were conducted. The crystals were cultured and obtained through slow evaporation of solvent, and the three molecules show highly twisted structures with large torsion angles between the electron donor and acceptor units (77.1° and 77.9° for IDP-*p*-PXZ, 77.1° and 82.0° for IDP-*p*-PTZ, and 75.5° and 89.1° for

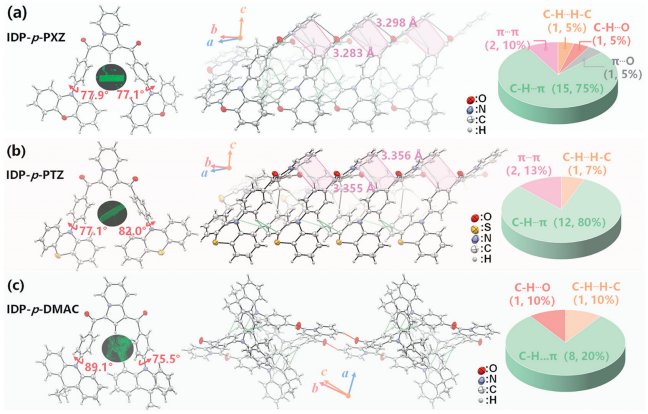


Fig. 1. Single crystal structures, dihedral angles, intermolecular interaction in the single crystals of (a) IDP-*p*-PXZ, (b) IDP-*p*-PTZ and (c) IDP-*p*-DMAC. Inset: Fluorescence microscopy photographs of the three crystals under 365 nm UV irradiation.

IDP-*p*-DMAC) (Fig. 1). This trend coincides well with the DFT results. The single-crystal data are summarized in Table S2 (Supporting information) and the intermolecular interactions and stacking patterns of the three target molecules in the crystals are exhibited in Fig. 1 and Figs. S5–S8 (Supporting information) IDP-*p*-PXZ and IDP-*p*-PTZ both are monoclinic system with the space group C2/c and showed similar stacking modes in molecular dimers. Notably, along crystallographic *b* axis, a typical step-like packing structure was observed in IDP-*p*-PXZ and IDP-*p*-PTZ, where molecules are parallel to each other into dimers based on strong intermolecular $\pi\cdots\pi$ stacking interactions between indolizine skeletons, along with multiple intermolecular C–H$\cdots\pi$ interactions (Figs. 1a and b). The difference in the radius of the S and O atom in the donor unit leads to the less planar nature of the PTZ compared to that in PXZ, resulting in a similar crystal structure but slightly different in donor planarity. In sharp contrast, IDP-*p*-DMAC is a triclinic system with P-1 space group, and only weak intermolecular C–H$\cdots\pi$ interactions existed in anti-parallel packed dimers between adjacent molecules (Fig. 1c). As to the intermolecular interactions and packing patterns, all the three crystals possessed abundant short contacts. IDP-*p*-PXZ has more intermolecular interactions due to the presence of multiple $\pi\cdots\pi$ stacking, C–H$\cdots\pi$ and O$\cdots\pi$ interactions, and as well as C–H$\cdots$O and C–H$\cdots$H–C hydrogen bonds, rendering faint emissions in the solid state. As to IDP-*p*-PTZ, it displayed similar but slightly weaker $\pi\cdots\pi$ stacking, C–H$\cdots\pi$ and C–H$\cdots$H–C hydrogen bonds. In contrast, the intermolecular interactions were significantly decreased in the crystals of IDP-*p*-DMAC with less C–H$\cdots\pi$, C–H$\cdots$O and C–H$\cdots$H–C hydrogen bonds, which might be caused by the methyl groups in the DMAC donor, leading to a loose packing mode. Thus, abundant intermolecular interactions such as $\pi\cdots\pi$ stacking result in a more compact stacking pattern for IDP-*p*-PXZ, suggesting its excellent PL performance, which is consistent with the fluorescence microscopy photographs.

The ultraviolet-visible (UV–vis) absorption spectra, fluorescence spectra, and corresponding transient PL spectra decay curves of the three molecules in toluene are shown in Fig. S9 (Supporting information), and the photophysical data are summarized in Table S3 (Supporting information). As shown in Figs. S9a–c, compounds IDP-*p*-PXZ, IDP-*p*-PTZ, and IDP-*p*-DMAC all have strong absorption peaks at 340, 362, and 363 nm, respectively, which can be attributed to $\pi\rightarrow\pi^*$ transitions. The fluorescence spectra of IDP-*p*-PXZ, IDP-*p*-PTZ, and IDP-*p*-DMAC show green to yellow emissions with maximum emission peaks at 584, 592 and 537 nm, respectively. The transient fluorescence decay curves of the three molecules show second-order exponential decay, with the instantaneous component lifetime (τ_{PF})/delayed component lifetime (τ_{DF}) of IDP-*p*-PXZ being 7.48 ns/0.50 μs, IDP-*p*-PTZ 6.56 ns/0.33 μs, and IDP-*p*-DMAC 771 ns/6.78 μs (Figs. S9d–f), confirming their TADF characteristics at the molecular level.

These three emitters show broad PL bands in the thin film (Fig. S10 in Supporting information), and the energies of the lowest singlet and triplet state were estimated to be 2.47 and 2.42 eV for IDP-*p*-PXZ, 2.53 and 2.46 eV for IDP-*p*-PTZ, and 2.73 and 2.53 eV for IDP-*p*-DMAC. Thereby, the corresponding ΔE_{ST} values were calculated to be 0.05, 0.07, and 0.20 eV, respectively. Such small values of ΔE_{ST} favor ISC and RISC process. The emission spectra of the three emitters in toluene solutions under degassed and aerated conditions were measured (Fig. S11 in Supporting information). The fluorescence intensity of the degassed solution with argon became stronger than those under aerated conditions, which further confirmed that triplet states were involved in the emission process. Besides, the lifetime decay curves of these molecules were recorded at different temperature (Fig. S12 and Table S4 in Supporting information). With the increasing temperature from 100 K to 298 K, the ratios of the delayed components increase gradually, which confirms the thermal activated nature of these emitters.

Owing to the highly twisted architectures of the three compounds, the PL spectra of them in the tetrahydrofuran (THF)/water mixed system were measured to investigate their AIE properties (Fig. S13 in Supporting information). The PL emission of the three molecules in THF solution is relatively weak due to the twisted intramolecular charge transfer (TICT) effect [34,35]. However, when the volume ratio of water (f_w) in the mixed system was increased to 70 %, the PL intensity of the three compounds increased rapidly. This could be ascribed to the fact that when the TADF molecules formed aggregates, intramolecular motion was restricted, blocking non-radiative decay channels, thus causing the PL intensity to increase [23]. Additionally, IDP-*p*-DMAC showed a blue shift and an increase in fluorescence intensity with water fraction of 95 %. The aggregates formed excluded most large polar solvent molecules, thereby weakening the intramolecular charge transfer (ICT) process. These results indicate that all the three molecules possess distinct distinctive AIE characteristics.

Most TADF molecules show poor water solubility owing to the purely organic structures, which restricts their direct application in biomedicine. To endow the TADF emitters with better water-dispersibility and improved bioavailability, the three molecules were then fabricated into corresponding NPs named IDP-*p*-PXZ NPs, IDP-*p*-PTZ NPs, and IDP-*p*-DMAC NPs using DSPE-PEG2000. First, the UV–vis absorption spectra, PL spectra and the transient PL decay curves of these three TADF NPs dispersed in ultrapure (UP) water, and the key photophysical data are summarized in Table 1. As shown in Fig. S14 (Supporting information), the three TADF NPs exhibited similar strong absorption bands around 370 nm, for which corresponds to the π-π^* electronic transition, while the weak and broad absorption band in the range of 460–520 nm can be attributed to the charge-transfer (CT) transition from the donors to the indolizine-benzophenone acceptor. Compared to the emission in toluene solutions, the emission spectra of the three TADF NPs in UP water were blue-shifted to a green or blue color. Noticeably, the transient fluorescence decay of the three TADF NPs in air showed obvious biexponential decay with τ_{PF}/τ_{DF} of IDP-*p*-PXZ NPs being 15.73 ns/0.58 μs, IDP-*p*-PTZ NPs 48.19 ns/0.67 μs, and IDP-*p*-DMAC NPs 17.33 ns/24.49 μs, along with the delayed fluorescence ratios of 48.1 %, 25.4 %, and 49.1 %, respectively (Figs. S14d–f). These results show that the three TADF NPs established an oxygen-insulated environment for the embedded TADF luminophore, providing a powerful way to protect the T_1 state from the quenching by oxygen. As shown in Table 1, in the case of the NP systems, the ISC rate constant (k_{ISC}) and radiative rate constant (k_r) in air were estimated to be 3.40×10^7 $s^{-1}/5.05\times10^6$ s^{-1}, 1.88×10^7 $s^{-1}/0.83\times10^6$ s^{-1}, and 2.94×10^7

Table 1
Photophysical data of IDP-*p*-PXZ NPs, IDP-*p*-PTZ NPs and IDP-*p*-DMAC NPs. Measured in UP water (10^{-5} mol/L) at room temperature.

Compound	λ_{abs} (nm)	λ_{em} (nm)	τ_{PF} (ns) [a]	τ_{DF} (μs) [a]	$\Phi/\Phi_p/\Phi_d$ [b]	k_p ($\times 10^7$ s^{-1}) [c]	k_d ($\times 10^5$ s^{-1}) [c]	k_r ($\times 10^6$ s^{-1}) [d]	k_{ISC} ($\times 10^7$ s^{-1}) [e]	k_{RISC} ($\times 10^5$ s^{-1}) [e]
IDP-*p*-PXZ NPs	365	520	15.73	0.58	16/8.3/7.7	6.37	17.36	5.05	3.40	35.05
IDP-*p*-PTZ NPs	375	547	48.19	0.67	13/9.7/3.3	2.08	14.93	0.83	1.88	48.54
IDP-*p*-DMAC NPs	365, 490	479	17.33	24.49	11/5.6/5.4	5.78	0.41	3.12	2.94	0.83

[a] The lifetimes of prompt and delayed fluorescence in air.
[b] The total, prompt and delayed fluorescence PLQY in air.
[c] The rate constants of prompt and delayed radiation.
[d] The radiative rate constants of the singlet state.
[e] The rate constants of the ISC and RISC processes.

$s^{-1}/3.12 \times 10^6$ s^{-1}, respectively. The simultaneous rapid ISC rate and efficient radiative decay ensures efficient ROS generation and bright emission, shedding light on their potential for PDT and cellular imaging applications.

We first investigated the ROS type and generation ability of the three TADF NPs with commercial fluorescent probe singlet oxygen sensor green (SOSG) under 520 nm laser irradiation (30 mW/cm^2). SOSG is a probe highly selectively binds to $^1O_2$ and has no obvious reaction to hydroxyl radical (OH$^\bullet$), superoxide anion radical (O_2^{-}) and nitric oxide (NO). The SOSG itself exhibits a faint blue fluorescence, but upon reaction with singlet oxygen, the resulting intra-SOSG peroxide (SOSG-EP) fluoresces green ($\lambda_{em} = 525$ nm). The more the singlet oxygen generated, the more the intensity of fluorescence increased. As shown in Fig. S20 (Supporting information), the three TADF NPs display excellent ROS generation ability under laser irradiation, and with the increase of irradiation time (0–20 min), the fluorescence intensity of the three TADF NPs + SOSG increased by 2.5–5.9 times. For a control sample with none of the TADF NPs, SOSG shows no observable emission upon irradiation for 20 min. In addition, in the presence of H_2O or TADF NPs, the fluorescence intensities of SOSG did not change without laser irradiation (Fig. S21 in Supporting information). These results suggested that the three TADF NPs were capable of generating $^1O_2$ effectively through type-II process. IDP-*p*-PXZ NPs + SOSG initially exhibited higher fluorescence intensity which may be related to its relatively faster ISC rate (Table 1). Notably, the emission intensity of IDP-*p*-DMAC NPs + SOSG rose to nearly 14.7 folds higher than the initial intensity after 20 min 520 nm laser irradiation. This is in accordance with its fast ISC rate and extremely slow RISC rate, contributing to retaining the TADF NPs in the excited T_1 state for $^1O_2$ generation by preventing the RISC process. Subsequently, we employed 2′,7′-dichlorofluorescein diacetate (DCFH-DA) as an intracellular ROS detection probe to investigate the effects of the concentrations of TADF NPs in HeLa cells. Different concentrations of the three TADF NPs were co-cultured with HeLa cells for 12 h, subsequent treatment with DCFH-DA for 20 min, and exposure to a 520 nm laser for another 20 min resulted in a detectable DCF green fluorescence. As depicted in Fig. S22 (Supporting information), with no NPs, green fluorescence from DCF could not be detected. As the concentration of the three TADF NPs increased, the green fluorescence from DCF increased, resulting a concentration-dependent ROS generation. These results suggest that the three TADF NPs have a remarkable capability for ROS generation and thus good potential for PDT applications. Furthermore, to compare the $^1O_2$ generation abilities of the three TADF NPs, the quantum yield (Φ) of ROS for NPs were determined by using 1,3-diphenylisobenzofuran (DPBF) as an indicator and rose bengal (RB) as a standard reference (Figs. S23 and S24 in Supporting information) [21]. The Φ_{NPs} of the IDP-*p*-PXZ NPs, IDP-*p*-PTZ NPs, and IDP-*p*-DMAC NPs were determined to be 0.397, 0.399, and 0.524, respectively.

We further examined the cytotoxicity of the three TADF NPs within a concentration range of 0−100 μmol/L without laser irradiation. Fig. 2a demonstrates that cell viability of IDP-*p*-PXZ NPs

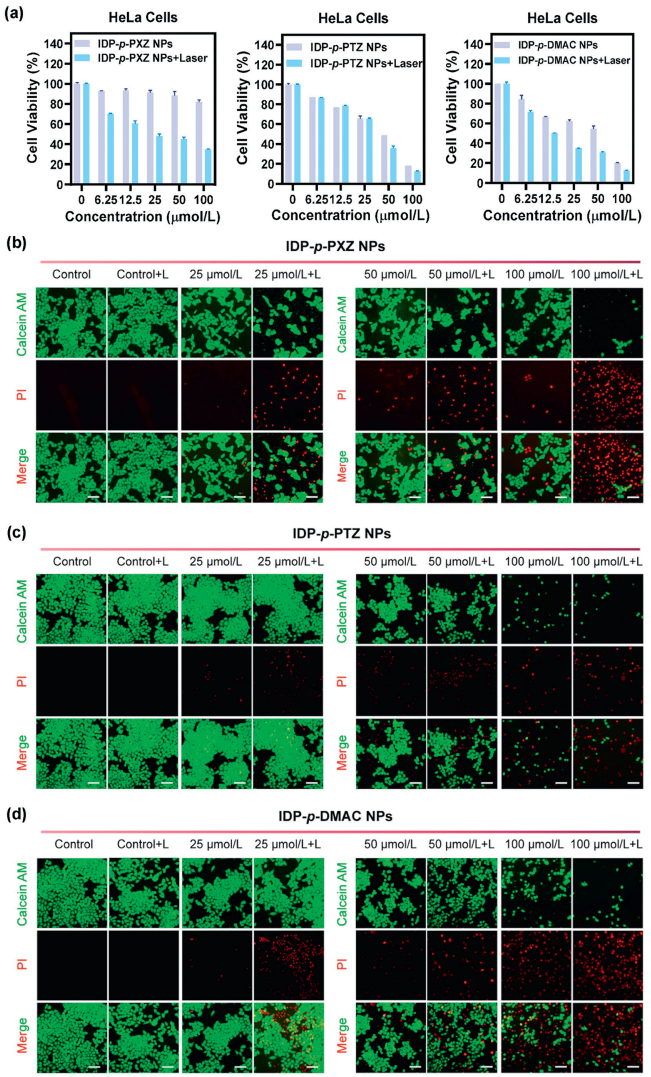


Fig. 2. (a) *In vitro* cytotoxicity of IDP-*p*-PXZ NPs, IDP-*p*-PTZ NPs and IDP-*p*-DMAC NPs in HeLa cells with or without visible light irradiation ($\lambda = 520$ nm, 30 mW/cm^2, 20 min; $n \geq 3$). Error bars indicate standard deviation (SD). The live/dead staining of HeLa cells receiving different treatments of (b) IDP-*p*-PXZ NPs. (c) IDP-*p*-PTZ NPs and (d) IDP-*p*-DMAC NPs with or without laser ($\lambda = 520$ nm). Scale bar: 50 μm.

was not significantly affected, which indicated its good cellular biocompatibility. Subsequently, upon exposure to green light irradiation ($\lambda = 520$ nm, 30 mW/cm^2, 20 min), at a concentration of 100 μmol/L, the growth inhibition ratio was determined to be 65% for IDP-*p*-PXZ NPs, confirming the PDT effect of IDP-*p*-PXZ NPs in HeLa cells. In sharp contrast, both IDP-*p*-PTZ NPs and IDP-*p*-DMAC NPs showed obvious cytotoxicity as the concentration increased even without laser exposure, which limits their *in vitro* and *in vivo* applications for PDT. The cytotoxic effect of IDP-*p*-PTZ NPs was espe-

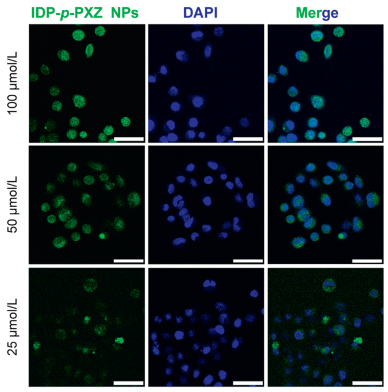


Fig. 3. Confocal fluorescence and merged images of HeLa cells with different concentrations (25, 50, and 100 μmol/L) of IDP-*p*-PXZ NPs in DMEM medium (excitation: 488 nm, emission: 550–600 nm). The nuclei were stained with DAPI (excitation: 330 nm, emission: 430–450 nm, scale bar: 50 μm).

cially registered, which was greatly affected by the donor PTZ, for a series of similar indolizine-phenothiazine hybrids were reported to have promising antitumor activity and display cytotoxicity potential with growth inhibition 50 % (GI_{50}) values in the low nanomolar range in several cancer cells [32]. The dark toxicity of IDP-*p*-DMAC NPs might be driven by its long-lived triplet states (promoting $^1O_2$) and structural instability (releasing toxic radicals).

To visualize the *in vitro* PDT effect of the three TADF NPs, we carried out the calcein-AM (green emission, live cells) and propidium iodide (PI, red emission, dead cells) staining assay. As shown in Figs. 2b–d, all the images of control groups (without light or TADF NPs) were fully covered with living cells. On the contrary, HeLa cells treated with both light and TADF NPs showed increasing toxicity with increasing TADF NPs concentration under laser irradiation for 20 min. Among the three TADF NPs, IDP-*p*-PXZ NPs has the best biocompatibility and PDT effect, which is in good agreement with its DFT calculations and photophysical property results. IDP-*p*-PXZ demonstrated the smallest ΔE_{ST} value, largest spin-orbital coupling constant and rapid ISC rate, upon laser excitation, IDP-*p*-PXZ NPs are excited by photons to the S_1 state and then reaches the T_1 state through an effectual ISC process, which transfers energy to the surrounding ground $^3O_2$, leading to the formation of cytotoxic $^1O_2$ [13].

Motivated by the favorable biocompatibility and robust fluorescence emission of IDP-*p*-PXZ NPs, we further explored its effectiveness in fluorescence imaging *in vitro*. We prepared different concentrations of IDP-*p*-PXZ NPs in culture medium, and HeLa cells were cultured for 6 h with IDP-*p*-PXZ NPs and observed under an inverted fluorescence imaging system. We stained the cell nuclei with anti-fluorescence quenching solution (containing 4′,6-diamidino-2-phenylindole (DAPI)) to study the cellular uptake efficiency of IDP-*p*-PXZ NPs in HeLa cells. The prepared IDP-*p*-PXZ NPs were successfully internalized by the cells and displayed bright and stable green fluorescence under 488 nm excitation. The cellular uptake of IDP-*p*-PXZ NPs by HeLa cells showed a concentration-dependent trend, and endocytosis of the material at 25 μmol/L in cells was clearly detected (Fig. 3 and Fig. S25 in Supporting information). These results revealed that the IDP-*p*-PXZ NPs achieved stable and unquenchable fluorescence as well as excellent biocompatibility for cell imaging, showcasing their immense potential as a theranostic platform, combining PDT and imaging functionalities in a single system.

In summary, we develop a new series of indolizine-benzophenone based electron-deficient acceptor to construct three AIE-active TADF molecules (IDP-*p*-PXZ, IDP-*p*-PTZ, and IDP-*p*-DMAC) with D–A–D architectures. By systematically altering the donor units, we elucidated the pivotal role of donor engineering in modulating excited-state dynamics, crystal packing, and photophysical properties. Upon encapsulation into NPs, the three TADF NPs exhibited oxygen-insensitive behavior and demonstrated exceptional ROS generation efficiency under laser irradiation. Compared to recently reported AIE-TADF materials for photodynamic therapy (Table S6 in Supporting information) [21,36–40], our TADF NPs demonstrates a balanced performance: (i) A relatively high PLQY (11 %–16 % in air) addressing the common fluorescence quenching issue in aggregated AIE-TADF systems (typically <10 %), (ii) outstanding Φ_{ROS} (39 %–52 %), surpassing most heavy-atom-free alternatives, and (iii) biocompatible green-light activation ($\lambda_{ex} = 520$ nm, 30 mW/cm^2). Among the three emitters, IDP-*p*-PXZ NPs emerged as the most promising candidate, characterized by its minimized ΔE_{ST}, low cytotoxicity, enhanced SOCME, rapid ISC rate, and efficient radiative decay. These properties enabled simultaneous confocal fluorescence imaging and PDT *in vitro*. This work highlights the structural merits of the indolizine-benzophenone acceptor in advancing AIE-TADF materials, achieving exceptional ROS generation and biocompatibility, and thus paving the way for innovative applications in PDT and bioimaging.

Declaration of competing interest

The authors declare that they have no known competing financial interests or personal relationships that could have appeared to influence the work reported in this paper.

CRediT authorship contribution statement

Hui Guo: Writing – original draft, Validation, Formal analysis, Data curation. **Wen-Wen Li:** Validation, Data curation. **Mei-Yin Wu:** Validation, Data curation. **Jian-Bo Hu:** Data curation. **Jun Wang:** Data curation. **Yun Liu:** Writing – review & editing, Funding acquisition. **Yang Zou:** Writing – review & editing. **Chu-Luo Yang:** Writing – review & editing, Investigation, Funding acquisition. **Kai-Lu Zheng:** Writing – review & editing, Writing – original draft, Supervision, Investigation, Funding acquisition, Data curation.

Acknowledgments

This work was supported by the National Natural Science Foundation of China (No. 22405062), the Guangdong Basic and Applied Basic Research Foundation (No. 2021A1515110869), the Shenzhen Science and Technology Program (No. ZDSYS20210623091813040), Innovation Program of Zhanjiang (No. 2020LHJH005), and Funds for Ph.D. researchers of Guangdong Medical University in 2025 (No. 4SG25007G). The authors thank Prof. Fan Ni (Hefei University of Technology) for the helpful suggestion on theoretical calculations. The authors thank Prof. Shao-Long Gong (Wuhan University) for transient fluorescence spectroscopy measurement.

Supplementary materials

Supplementary material associated with this article can be found, in the online version, at doi:10.1016/j.cclet.2025.111721.

References

[1] Z. Yang, Z. Mao, Z. Xie, et al., Chem. Soc. Rev. 46 (2017) 915–1016.
[2] B. Zhou, D. Ya, Adv. Funct. Mater. 29 (2019) 1807599.
[3] B. Zhou, Z. Qi, M. Dai, C. Xing, D. Yan, Angew. Chem. Int. Ed. 62 (2023) e202309913.
[4] F. Ni, Y. Huang, L. Qiu, C. Yang, Chem. Soc. Rev. 53 (2024) 5904–5955.
[5] T. Hua, X. Cao, J. Miao, et al., Nat. Photon. 18 (2024) 1161–1169.
[6] B.T. Luppi, W.L. Primrose, Z.M. Hudson, Angew. Chem. Int. Ed. 63 (2024) e202400712.
[7] J.R. Caine, P. Hu, A.T. Gogoulis, Z.M. Hudson, Acc. Mater. Res. 4 (2023) 879–891.

[8] K.W. Lee, Y. Wan, Z. Huang, et al., Adv. Mater. 36 (2024) 2306492.
[9] W. Chen, F. Song, Chin. Chem. Lett. 30 (2019) 1717–1730.
[10] Z. Li, X.G. Yang, H. Zhang, et al., Inorg. Chem. Front. 9 (2022) 4281–4287.
[11] S. Xu, Q. Zhang, X. Han, et al., ACS Sens. 5 (2020) 1650–1656.
[12] N.R. Paisley, S.V. Halldorson, M.V. Tran, et al., Angew. Chem. Int. Ed. 60 (2021) 18630–18638.
[13] W. Fan, P. Huang, X. Chen, Chem. Soc. Rev. 45 (2016) 6488–6519.
[14] R. Gao, X. Mei, D. Yan, R. Liang, M. Wei, Nat. Commun. 9 (2018) 2798.
[15] F. Ni, N. Li, L. Zhan, C. Yang, Adv. Opt. Mater. 8 (2020) 1902187.
[16] T. Hu, L. Yan, Z. Wang, et al., Chem. Sci. 12 (2021) 2594–2603.
[17] N. Guo, Y. Xia, Y. Duan, et al., Chin. Chem. Lett. 34 (2023) 107542.
[18] P.P. Singh, S. Sinha, P. Gahtori, et al., Dyes Pigm. 229 (2024) 112262.
[19] M. Chen, Z. Zhang, R. Lin, et al., Chem. Sci. 15 (2024) 6777–6788.
[20] F. Fang, L. Zhu, M. Li, et al., Adv. Sci. 8 (2021) 2102970.
[21] S. Hu, B. Huang, Y. Pu, et al., J. Mater. Chem. B 9 (2021) 5645–5655.
[22] W. Chen, Z. Wang, M. Tian, et al., J. Am. Chem. Soc. 145 (2023) 8130–8140.
[23] S. Li, Y. Lin, D. Yan, J. Mater. Chem. C 4 (2016) 2527–2534.
[24] H. Zhang, C. He, L. Shen, et al., Chin. Chem. Lett. 34 (2023) 108160.
[25] F. Song, X. Ou, T.Y. Chou, et al., ACS Nano 16 (2022) 6176–6184.
[26] H. Zhao, N. Li, C. Ma, et al., Chin. Chem. Lett. 34 (2023) 107699.
[27] Y.Z. Shi, Y.F. Xiao, H. Wu, et al., CCS Chem. 6 (2024) 912–922.
[28] J.Q. Feng, X. Tian, R.G. Cao, et al., Chin. Chem. Lett. 35 (2024) 109657.
[29] Z. Li, J. Song, X. Gao, et al., Chin. Chem. Lett. 36 (2025) 110073.
[30] Y.M. Shen, P.C. Lv, W. Chen, et al., Eur. J. Med. Chem. 45 (2010) 3184–3190.
[31] A. Ghinet, C.M. Abuhaie, P. Gautret, et al., Eur. J. Med. Chem. 89 (2015) 115–127.
[32] I.M. Moise, E. Bîcu, A. Farce, J. Dubois, A. Ghinet, Bioorg. Chem. 103 (2020) 104184.
[33] W.M. Shu, J.X. He, X.F. Zhang, S. Wang, A.X. Wu, J. Org. Chem. 84 (2019) 2962–2968.
[34] F. Fang, Y. Yuan, Y. Wan, et al., Small 18 (2022) 2106215.
[35] S. Chen, H. Wang, Y. Hong, B.Z. Tang, Mater. Horiz. 3 (2016) 283–293.
[36] Y.F. Xiao, J.X. Chen, S. Li, et al., Chem. Sci. 11 (2020) 888–895.
[37] Y.F. Xiao, J.X. Chen, W.C. Chen, et al., Chem. Commun. 57 (2021) 4902–4905.
[38] Y.F. Xiao, W.C. Chen, J.X. Chen, et al., ACS Appl. Mater. Interfaces 14 (2022) 5112–5121.
[39] Q. Sha, X. Li, X. Gu, T. Yuan, J. Hua, Talanta 286 (2025) 127570.
[40] D. Barman, P. Rajamalli, A.P. Bidkar, et al., Small 21 (2025) 2409533.